1 **Fluorescence lidar observations of wildfire smoke inside cirrus: A contribution to smoke-**

2 **cirrus - interaction research**

3 Igor Veselovskii[1], Qiaoyun Hu[2], Albert Ansmann[3], Philippe Goloub[2], Thierry Podvin[2], Mikhail

4 Korenskiy[1]

5 *[1]Prokhorov General Physics Institute of the Russian Academy of Sciences, Moscow, Russia.*

6 *[2]Univ. Lille, CNRS, UMR 8518 - LOA - Laboratoire d'Optique Atmosphérique, Lille, 59000,*

7 *France*

8 *[3]Leibniz Institute for Tropospheric Research, Leipzig, Germany*

9 **Correspondence**: Igor Veselovskii (iveselov@hotmail.com)

10

11 **Abstract**

12 A remote sensing method, based on fluorescence lidar measurements, that allows to detect and to

13 quantify the smoke content in upper troposphere and lower stratosphere (UTLS) is presented.

14 The unique point of this approach is that, smoke and cirrus properties are observed in the same

15 air volume simultaneously. In the article, we provide results of fluorescence and

16 multiwavelength Mie-Raman lidar measurements performed at ATOLL observatory from

17 Laboratoire d'Optique Atmosphérique, University of Lille, during strong smoke episodes in the

18 summer and autumn seasons of 2020. The aerosol fluorescence was induced by 355 nm laser

19 radiation and the fluorescence backscattering was measured in a single spectral channel, centered

20 at 466 nm of 44 nm width. To estimate smoke properties, such as number, surface area and

21 volume concentration, the conversion factors, which link the fluorescence backscattering and the

22 smoke microphysical properties, are derived from the synergy of multiwavelength Mie-Raman

23 and fluorescence lidar observations. Based on two case studies, we demonstrate that the

24 fluorescence lidar technique provides possibility to estimate the smoke surface area

25 concentration within freshly formed cirrus layers. This value was used in smoke INP

26 parameterization scheme to predict ice crystal number concentrations in cirrus generation cells.

27

28 **Introduction**

29   Aerosol particles in the upper tropospheric and lower stratospheric (UTLS) height regime

30 play an important role in processes of heterogeneous ice formation, however our current

31 understanding of these processes is insufficient for a trustworthy implementation in numerical

Atmospheric
Chemistry
and Physics
Discussions

Open Access

EGU

32   weather and climate prediction models. The ability of aerosol particles to act as ice nucleating

33   particles (INP) depends on meteorological factors such as temperature and ice supersaturation (as

34   a function of vertical velocity) as well as on the aerosol type in the layer in which cirrus

35   developed (Kanji et al., 2017). Heterogeneous ice nucleation initiated by insoluble inorganic

36   materials such as mineral dust has been studied since a long time (e.g., DeMott et al 2010, 2015;

37   Hoose and Möhler, 2012; Murray et al., 2012; Boose et al., 2016; Schrod et al., 2017; Ansmann

38   et al. 2019b), while the potential of omnipresent organic particles, especially of frequently

39   occurring aged, long-range-transported wildfire smoke particles, to act as INP is less well

40   explored and thus not well understood (Knopf et al., 2018). Wildfire smoke can reach the lower

41   stratosphere via pyro-cumulonimbus (pyroCb) convection (Fromm et al., 2010; Peterson et al.,

42   2018, 2021; Hu et al., 2019; Khaykin et al., 2020) or via self-lifting processes (Boers et al.,

43   2010,Ohneiser et al., 2021). It is widely assumed that the ability of smoke particles to serve as

44   INP mainly depends on the organic material (OM) in the shell of the coated smoke particles

45   (Knopf et al., 2018), but may also depend on mineral components in the smoke particles (Jahl et

46   al., 2021). The ice nucleation efficiency may increase with increasing duration of the long-range

47   transport as Jahl et al. (2021) suggested. Disregarding the progress made in this atmospheric

48   research field during the last years, the link between ice nucleation efficiency and the smoke

49   particle chemical and morphological properties is still largely unresolved (China et al., 2017;

50   Knopf et al., 2018).

51   To contribute to the field of smoke-cirrus-interaction research, we present a remote

52   sensing method that allows us simultaneously to detect and quantify the smoke amount inside of

53   cirrus layers together with cirrus properties and to provide INP estimates in regions close to

54   cloud top where ice formation usually begins. The unique point of our approach is that, for the

55   first time, smoke and cirrus properties are observed in the same air volume simultaneously.

56   Recently, a first attempt (closure study) was performed to investigate the smoke impact on High

57   Arctic cirrus formation (Engelmann et al. 2021). However, the aerosol measurements had to be

58   performed outside the clouds layers, and then the assumption was needed that the found aerosol

59   (and estimated INP) concentration levels also hold inside the cirrus layers. Now, we are able to

60   directly determine INP-relevant smoke parameters inside the cirrus layer during ice nucleation

61   events. This also offers the opportunity to illuminate whether an INP reservoir can be depleted in

62   cirrus evolution processes or not. Furthermore, this new lidar detection method permits a clear

63   discrimination between, e.g., smoke and mineral dust INPs.

64   Multiwavelength Mie-Raman lidars or High Spectral Resolution lidars (HSRL) are

65   favorable instruments to profile the physical properties of aerosol particles in troposphere. In

66   particular, the inversion of so-called $3\beta+2\alpha$ lidar observations, based on the measurement of

67   height profiles of three aerosol backscatter coefficients at 355, 532, and 1064 nm and two

68   extinction coefficients at 355 and 532 nm, allows us to estimate smoke microphysical properties

69   (Müller et al., 1999, 2005; Veselovskii et al., 2002, 2015). However, the aerosol content in

70   UTLS height range can be low, so that particle extinction coefficients cannot be determined with

71   sufficient accuracy and are thus not available in the lidar inversion data analysis. To resolve this

72   issue Ansmann et al. (2019a, 2021) used the synergy of polarization lidar measurements and

73   Aerosol Robotic Network (AERONET) sunphotometer observations (Holben et al., 1998) to

74   derived conversion factors (to convert backscatter coefficients into microphysical particle

75   properties) and to estimate INP concentrations for dust and smoke aerosols with the retrieved

76   aerosol surface area concentration as aerosol input.

77   Dust particles are very efficient ice nuclei in contrast to wildfire smoke particles. In this

78   context, the question arises: How can we unambiguously discriminate smoke from dust

79   particles? This is realized by integrating a fluorescence channel into a multiwavelength aerosol

80   lidar (Reichardt et al., 2017; Veselovskii et al., 2020; 2021). The fluorescence capacity of smoke

81   (ratio of fluorescence backscattering to the overall aerosol backscattering), significantly exceeds

82   corresponding values for other types of aerosol, such as dust or anthropogenic particles

83   (Veselovskii et al., 2020; 2021), and thus allows us to discriminate smoke from other aerosol

84   types. The fluorescence technique provides therefore the unique opportunity to monitor ice

85   formation in well identified wildfire smoke layers, and thus to create a good basis for long-term

86   investigations of smoke cirrus interaction.

87   In this article, we present results of fluorescence and multiwavelength Mie-Raman lidar

88   measurements performed at the ATOLL (ATmospheric Observation at liLLe) at Laboratoire

89   d'Optique Atmosphérique, University of Lille, during strong smoke episodes in the summer and

90   autumn seasons of 2020. The results demonstrate that the fluorescence lidar is capable to monitor

91   the smoke in the UTLS height range and inside the cirrus clouds formed at or below the

92   tropopause. We start with a brief description of the experimental setup in Sect.2. In the first part

Atmospheric
Chemistry
and Physics
Discussions

Open Access

EGU

93   of the result section (Sect.3.1 and 3.2), it is explained how smoke optical properties can be
94   quantified by using fluorescence backscattering information and how we can estimate smoke
95   microphysical properties (volume, surface area, and number concentration) from measured
96   fluorescence backscatter coefficients. In this approach, multiwavelength Mie-Raman aerosol
97   lidar observations are used in addition. Values of the smoke particle surface area concentration
98   are then the aerosol input in the smoke INP estimation. A case study is discussed in Sect.3.2.
99   Two case studies are then presented in Sect.3.3 to demonstrate the capability of a fluorescence
100   lidar to monitor ice formation in extended smoke layers and to provide detailed information on
101   aerosol microphysical properties and smoke-relate INP concentration levels.

102

103   **2. Experimental setup**

104   The multiwavelength Mie-Raman lidar LILAS (LIlle Lidar AtmosphereS) is based on a
105   tripled Nd:YAG laser with a 20 Hz repetition rate and pulse energy of 70 mJ at 355 nm.
106   Backscattered light is collected by a 40 cm aperture Newtonian telescope and the lidar signals
107   are digitized with Licel transient recorders of 7.5 m range resolution, allowing simultaneous
108   detection in the analog and photon counting mode. The system is designed for simultaneous
109   detection of elastic and Raman backscattering, allowing the so called $3\beta+2\alpha+3\delta$ data
110   configuration, including three particle backscattering (β_{355}, β_{532}, β_{1064}), two extinction (α_{355}, α_{532})
111   coefficients along with three particle depolarization ratios (δ_{355}, δ_{532}, δ_{1064}). The particle
112   depolarization ratio, determined as a ratio of cross- and co-polarized components of the particle
113   backscattering coefficient, was calculated and calibrated in the same way as described in
114   Freudenthaler et al. (2009). The aerosol extinction and backscattering coefficients at 355 and 532
115   nm were calculated from Mie-Raman observations (Ansmann et al., 1992), while β_{1064} was
116   derived by the Klett method (Fernald, 1984; Klett, 1985). Additional information about
117   atmospheric parameters was available from radiosonde measurements performed at
118   Herstmonceux (UK) and Beauvechain (Belgium) stations, located 160 km and 80 km away
119   from the observation site respectively.

120   The lidar system is also capable to perform aerosol fluorescence measurements. A part of
121   the fluorescence spectrum is selected by a wideband interference filter of 44 nm width centered
122   at 466 nm (Veselovskii et al., 2020; 2021). The strong sunlight background at daytime restricts
123   the fluorescence observations to nighttime hours. To characterize the fluorescence properties of

124   aerosol, the fluorescence backscattering coefficient β_F is calculated from the ratio of

125   fluorescence and nitrogen Raman backscatters, as described in Veselovskii et al. (2020). This

126   approach allows to evaluate the absolute values of β_F, if the relative sensitivity of the channels is

127   calibrated and the nitrogen Raman scattering differential cross section σ_R is known. In our

128   research we used $\sigma_R=2.744*10^{-30}$ cm^{2}sr^{-1} at 355 nm from Venable et al. (2011). All β_F profiles

129   presented in this work were smoothed with the Savitzky – Golay method, using second order

130   polynomial with 21 points in the window. The efficiency of fluorescence backscattering with

131   respect to elastic backscattering β_{532} is characterized by the fluorescence capacity $G_F = \dfrac{\beta_F}{\beta_{532}}$.

132   For most of atmospheric particles β_F is proportional to the volume of dry matter, while

133   dependence of β_{532} on particle size is more complicated. As a result, G_F depends not only on

134   aerosol type, but also on particle size and the relative humidity RH. We recall also, that only a

135   part of the fluorescence spectra was selected by the interference filter in the receiver, so provided

136   values of β_F and G_F are specific for the filter used. Analyzing the fluorescence measurements we

137   should keep in mind, that the sensitivity of this technique can be limited by the fluorescence of

138   optics in the lidar receiver. The minimal value of G_F, which we measured during observation in

139   cloudy conditions in the lower troposphere was about 2×10^{-8}. Thus, at least, in the measurements

140   with G_F above this value, the contribution of optics fluorescence can be ignored.

141

142   **3. Results of the measurements**

143   *3.1. Observation of smoke particles in UTLS*

144   Smoke particles produced by intensive fires and transported across the Atlantic are

145   regularly observed in the UTLS height range over Europe (Müller et al., 2005; Hu et al., 2019;

146   Baars et al., 2019, 2021). One of such events, observed over Lille in the night of 4-5 November

147   2020, is shown in Fig.1. The figure provides height – time displays of the range corrected lidar

148   signal and the volume depolarization ratio at 1064 nm together with the fluorescence

149   backscattering coefficient. A narrow smoke layer occurred in the upper troposphere in the period

150   from 23:00 – 06:00 UTC. The smoke was detected at heights above 12 km after midnight. The

151   particles caused a low volume depolarization ratio (<5%) at 1064 nm and strong fluorescence

152   backscattering ($\beta_F>1.2\times10^{-4}$ Mm^{-1}sr^{-1}). The backward trajectory analysis indicated that the

153 aerosol layer was transported over the Atlantic and contained products of North American wild

154 fires.

155   Vertical profiles of aerosol β_{532} and fluorescence β_F backscattering coefficients for the

156 period from 02:00 - 05:30 UTC are shown in Fig.2a. The fluorescence capacity G_F in the center

157 of smoke layer (not shown) was about 4.5×10^{-4}. The depolarization ratio of aged smoke in the

158 UTLS height range usually shows a strong spectral dependence (Haarig et al., 2018; Hu et al.,

159 2019). For the case presented in Fig.2a the particle depolarization ratio in the center of the smoke

160 layer decreased from 16±4% at 355 nm (δ_{355}) to 4±1% at 1064 (δ_{1064}). The tropopause height H_{tr}

161 was at about 13000 m, thus the main part of the smoke layer was below the tropopause. By the

162 end of day the smoke layer became weaker ($\beta_F<0.3\times10^{-4}$ Mm^{-1}sr^{-1}) and ascended up to 14500 m,

163 which is above the tropopause. Corresponding vertical profiles of β_{532} and β_F are shown in

164 Fig.2b. The fluorescence capacity in the center of the layer is about 4.5×10^{-4}, which is close to

165 the value observed during 02:00 - 05:30 UTC period.

166   An important advantages of the fluorescence lidar technique is the ability to monitor

167 smoke particles inside cirrus clouds. The results of smoke observations in the presence of ice

168 clouds are shown in Fig.3. Cirrus clouds occurred during the whole night in the height range

169 from 6.0 km – 10.0 km. To quantify the fluorescence backscattering inside the cloud (which was

170 rather weak in this case), the lidar signals were averaged over the full 18:00 – 06:00 UTC time

171 interval in Fig.3a. The fluorescence backscatter coefficient shown in Fig.3c decreased from

172 $\beta_F=0.015\times10^{-4}$ Mm^{-1}sr^{-1} at 5000 m (near the cloud base) to a minimum value of 0.01×10^{-4} Mm^{-1}sr^{-1} at 7000 m inside the cirrus layer. Above the tropopause the fluorescence backscattering

174 increased strongly and reached the maximum (about 0.3×10^{-4} Mm^{-1}sr^{-1}) in 11000 m -13000 m

175 height.

176   The analysis of fluorescence measurements performed during strong smoke episodes in

177 the summer and autumn of 2020, when smoke layers from North American fires frequently

178 reached Europe, demonstrates that the fluorescence capacity varied within the range of 2.8×10^{-4}

179 to 4.5×10^{-4}. The variations are a function of smoke composition, relative humidity and particle

180 size. However, in the upper troposphere, where relative humidity is low, G_F was normally close

181 to 4.5×10^{-4}. This relatively low range of G_F variations allows the estimation of the backscattering

182 coefficient attributed to the smoke particles from fluorescence measurements as:

183
$$\beta_{532}^s = \frac{\beta_F}{G_F}.$$
(1)

184   Fig.3d shows the smoke backscattering coefficient β_{532}^s, calculated from β_F for

185     $G_F=4.5\times10^{-4}$, together with β_{532}. The dynamical range of β_{532} variations is high. To make smoke

186   backscattering visible above H_{Tr}, β_{532} is plotted in expanded scale in Fig.3d. The β_{532}^s values,

187   though being strongly oscillating above the tropopause, match the β_{532} indicating that the smoke

188   contribution to backscattering was predominant.

189

190   **3.2. Estimation of smoke particles content based on fluorescence measurements**

191   The possibility to detect fluorescence backscattering inside the cirrus clouds reveals also

192   the opportunity for a quantitative characterization of the smoke content. This can be realized by a

193   synergistic use of fluorescence and multiwavelength Mie – Raman lidar observations. For the

194   smoke layers with sufficient optical depth, the number N, surface area S and volume V

195   concentrations can be evaluated, by inverting the $3\beta+2\alpha$ observations consisting of three

196   backscatter coefficients (355, 532, 1064 nm) and two extinction coefficients (355, 532 nm)

197   (Müller et al., 1999; Veselovskii et al., 2002). The conversion factors C_N, C_S, C_V, introduced as

198     $$C_N = \frac{N}{\beta_F}, \ C_S = \frac{S}{\beta_F}, \ C_V = \frac{V}{\beta_F},$$
(3)

199   allow the estimation of N, S, and V from fluorescence backscattering.

200   On 23-24 June 2020, a strong smoke layer was observed in $4500 – 5500$ m height during

201   the whole night (Fig.4). The vertical profiles of the aerosol backscattering and extinction

202   coefficients ($3\beta+2\alpha$) are shown in Fig.5a, while the particle depolarization ratios δ_{355}, δ_{532}, δ_{1064}

203   and the lidar ratios at 355 nm and 532 nm (LR_{355}, LR_{532}) are presented in Fig.5b. The

204   depolarization ratio decreases with wavelength from $9\pm1.5\%$ at 355 nm to $1.5\pm0.3\%$ at 1064 nm

205   and the lidar ratio at 532 nm significantly exceeds corresponding value at 355 nm (80 ± 12 sr and

206   50 ± 7.5 sr respectively), which is typical for aged smoke (Müller et al., 2005). The

207   multiwavelength observations were inverted to determine the particle effective radius r_{eff},

208   number, surface area and volume concentrations for seven height bins inside the smoke layer.

209   The effective radius r_{eff} in Fig.5c increases through the layer from 0.15 µm to 0.2 µm

210   simultaneously with the increase of the fluorescence capacity G_F from 2.8×10^{-4} to 3.6×10^{-4}.

211   Retrieved values of N, S, V were used for calculation of conversion factors (Eq. 3) for each

212   height bin. In the center of the smoke layer (at 4.9 km) the factors are: $C_N = 88 \times 10^4 \dfrac{cm^{-3}}{Mm^{-1}sr^{-1}}$,

213    $C_S = 35 \times 10^4 \dfrac{\mu m^2 cm^{-3}}{Mm^{-1}sr^{-1}}$, and $C_V = 2.4 \times 10^4 \dfrac{\mu m^3 cm^{-3}}{Mm^{-1}sr^{-1}}$. Thus, when β_F is given in Mm^{-1}sr^{-1}, the

214   calculated values of N, S, and V are given in cm^{-3}, μm^{2}cm^{-3} and μm^{3}cm^{-3} respectively.

215   Fluorescence backscattering is proportional to the particle volume concentration, so C_V is not

216   sensitive to the effective radius variation. The conversion factors C_N and C_S, on the contrary,

217   depend on the particle size. Fig.5d shows the profiles of N, S, V obtained by inversion of 3β+2α

218   observations (symbols) together with corresponding values (N_F, S_F, V_F) obtained from β_F, using

219   the mean conversion factors for seven height bins considered. The volume concentrations V and

220   V_F agree well for all seven height bins. For the surface area concentrations the agreement is still

221   good, but for N and N_F the difference is up to 30%. We need to emphasize, that the conversion

222   factors presented are specific for our lidar system (for the interference filter installed in

223   fluorescence channel). It is worthwhile to mention that the ratio V/α_{532} of the volume

224   concentration V in Fig.5d to the extinction coefficient α at 532 nm in Fig.5a, as well as the ratio

225   S/α_{532}, are very close to respective extinction-to-volume and extinction-to-surface-area-

226   concentration conversion factors presented for aged wildfire smoke by Ansmann et al. (2021).

227   The conversion factors depend on the smoke composition. To estimate the variation range

228   of C_N, C_S, C_V, several smoke episodes were analyzed and corresponding results are presented in

229   Table 1. The table provides the fluorescence capacity G_F and the conversion factors at the

230   heights, where 3β+2α data could be calculated. Mean values of C_N, C_S, C_V derived for these

231   episodes and corresponding standard deviations are:

232    $C_N = (61 \pm 32) \times 10^4 \dfrac{cm^{-3}}{Mm^{-1}sr^{-1}}$; $C_S = (28 \pm 6.4) \times 10^4 \dfrac{\mu m^2 cm^{-3}}{Mm^{-1}sr^{-1}}$; $C_V = (2.2 \pm 0.2) \times 10^4 \dfrac{\mu m^3 cm^{-3}}{Mm^{-1}sr^{-1}}$ (4)

233   Thus, the expected uncertainties in the N, S and V estimations from fluorescence measurements

234   are of 50%, 25%, and 10% respectively, which is comparable with uncertainty of inversion of

235   3β+2α observations (Veselovskii et al., 2002; Pérez-Ramírez et al., 2013). Table 1 shows also

236   the volume and surface area concentrations of the smoke particles obtained from the inversion of

237   *3β+2α* observations (*V*, *S*) and calculated from β_F (*V$_F$*, *S$_F$*) using the conversion factors in Eq.

Atmospheric
Chemistry
and Physics
Discussions

Open Access
EGU

238   (4). Standard deviations of V_F and S_F from corresponding values of $V_{3\beta+2\alpha}$ and $S_{3\beta+2\alpha}$ are 10% and

239   25% respectively.

240   The conversion factors in Eq. (4) are now used to estimate the smoke microphysical

241   properties inside the cloud, assuming in addition that the predominant contribution to the

242   fluorescence is provided by the smoke. Table 2 summarizes the number, surface area, and

243   volume concentrations of smoke particles inside the ice clouds, estimated from fluorescence

244   measurements for four episodes considered in this paper. On September 12-13, 2020, the smoke

245   layer with high fluorescence and low depolarization ratio at 1064 nm (below 4%) was observed

246   during the whole night inside the 2.0 km – 5.0 km height range. The cirrus cloud occurred above

247   11000 m also during the whole night. Fig.6a presents vertical profiles of the aerosol β_{532} and

248   fluorescence β_F backscattering coefficients. Fluorescence backscattering shows a maximum at

249   3.5 km, but it is detected even inside the cloud. The smoke backscattering coefficient β_{532}^s,

250   computed from β_F for $G_F=3.6\times10^{-4}$ agrees well with β_{532} inside the 2.0 – 10.0 km height range

251   (Fig.6b). The height profile of the surface area concentration of the smoke particles, calculated

252   from β_F using the respective conversion factor in Eq. (4), is shown in Fig.6c. In the smoke layer,

253   S is up to 60 $\mu m^2/cm^3$, while in the center of the cloud in 12 km – 13 km height the average value

254   of S is 1.6 ± 0.4 $\mu m^2/cm^3$. Corresponding values of number and volume concentrations in the

255   cloud center are 3.5 ± 1.8 cm^{-3} and 0.13 ± 0.013 $\mu m^3/cm^3$.

256   The temperature in the cloud ranged from about -50°C to almost -70°C and was -68°C at

257   cirrus top in Fig.6b where ice nucleation usually starts. We applied the immersion freezing INP

258   parameterization of Knopf and Alpert (2013) for Leonardite (a standard humic acid surrogate

259   material) and assume that this humic compound represents the amorphous organic coating of

260   smoke particles. The INP parameterization for smoke particles is summarized for lidar

261   applications in Ansmann et al. (2021). The selected parameterization allows the estimation of the

262   INP concentration as a function of ambient air temperature (freezing temperature), ice

263   supersaturation, particle surface area, and time period for which a certain level of ice

264   supersaturation is given. We simply assume a constant ice supersaturation of around 1.45 during

265   a time period of 600 s (upwind phase of a typical gravity wave in the upper troposphere). The

266   temperature at cirrus top height is set to -68°C and the aerosol surface area concentration to 2.0

267   $\mu m^2/cm^3$ as indicated in Fig.6c. The obtained INP concentrations of 1-10 L^{-1} for these

268   meteorological and aerosol environmental conditions can be regarded as the predicted number

269   concentration of ice crystals nucleated in the cirrus top region. Ice crystal number concentration

270   of 1-10 L^{-1} are typical values in cirrus layers when heterogeneous ice nucleation dominates. It

271   should be mentioned that the required very high ice supersaturation levels of close to 1.5 (ice

272   supersaturation of 1.1-1.2 is sufficient in case of mineral dust particles) are still lower than the

273   threshold supersaturation level of >1.5 at which homogeneous freezing starts to dominate. At

274   low updraft velocities around 10-25 cm/s, as usually given in gravity waves in the upper

275   troposphere (Barahona et al., 2017), heterogeneous ice nucleation very likely dominates the ice

276   production when cirrus evolves in detected aerosol layers.

277

278   ***3.3. Ice formation inside the smoke layers***.

279   During September 2020 we observed several episodes with ice cloud formation inside of

280   smoke layers. One of such episodes occurred on 11-12 September 2020 and is shown in Fig.7.

281   The height – time display of the fluorescence backscattering coefficient reveals the smoke layer

282   in the 5.0 - 10.0 km height range. Inside this layer, we can observe a short time interval of 15

283   minutes with a strongly increased depolarization ratio around 10.5 km height (red spots),

284   indicating ice cloud formation. Fig.8 shows vertical profiles of the aerosol backscattering

285   coefficients β_{355}, β_{532}, and β_{1064} as well the particle depolarization ratios δ_{355}, δ_{532}, and δ_{1064} for

286   two temporal intervals. The first interval (23:00 – 00:30 UTC) is prior to ice cloud formation and

287   the second one (01:20 – 01:45 UTC) covers ice occurrence period. The depolarization ratios at

288   all three wavelengths were < 5% below 6 km height. Above that height δ_{355} significantly

289   increased reaching the value of 10% at 7 km (Fig.8b), which is indicative of a change of the

290   particle shape (from spherical to irregular shape). The fluorescence capacity also changed with

291   height, being about $G_F=4.5\times10^{-4}$ at 5.5 km and it decreases to 3.5×10^{-4} by 8 km. The profile of

292   β_{532}^s shown in Fig.8c is calculated assuming $G_F=4.0\times10^{-4}$ and it matches well the profile of β_{532}

293   for the whole height range. The aerosol layer at 10.5 km is thus a pure smoke layer. Ice

294   formation at 10.5 km (Fig.8d-f) leads to a significant increase of β_{532} while β_{532}^s (or the

295   respective fluorescence backscatter coefficient β_F) remains low and at the same level as observed

296   below the cirrus layer, i.e., below 10 km height. The depolarization ratios at all three

297   wavelengths increases to typical cirrus values around 40%. The temperature at 10.5 km is about -

298   50 °C, and the surface area concentration of the smoke particles inside the cloud, estimated from

299   β_F, is about 10 µm^2/cm^3 (see Fig.8f, thin blue line). For these temperature and aerosol conditions

300   we yield smoke INP concentrations of 1-10 L^{-1} for ice supersaturation values even below 1.4

301   (1.38-1.4) and updraft duration of 600 s. When comparing Fig.8c and 8f at cirrus level it seems

302   to be that ice nucleation on the smoke particles widely depleted the smoke INP reservoir.

303   Another case of ice formation in the smoke layer was observed on 17-18 September

304   2020. Strong smoke layers occurred in the 5.0 km – 9.0 km height range as shown in Fig.9.

305   During the period from 22:30 – 00:00 UTC, the depolarization increased at 8.5 km height,

306   indicating ice formation. Vertical profiles of the particle parameters prior and during ice

307   formation are shown in Fig.10. The β^s_{532} calculated for G_F=3.5×10^{-4} matches well with β_{532}

308   below 6.9 km and above 8.0 km (Fig.10c), but inside the 7.0 km – 8.0 km height range

309    $\beta_{532} > \beta^s_{532}$, meaning that G_F was decreased. The depolarization ratio in the 7.0 km – 8.0 km

310   height range shows some enhancement (Fig.10b): in particular, δ_{532} increased from 10% to 12%.

311   Cloud formation at 8.5 km (Fig.10d) led to a significantly smaller increase of the depolarization

312   ratio, compared to the case on 11-12 September. Prior to the cloud formation the values of δ_{1064},

313   δ_{532}, and δ_{355} at 8.5 km were of 3%, 10%, and 13% respectively (Fig.10b) and in the cloud

314   corresponding depolarization ratios increase up to 9%, 15%, 20%. The reason is probably that

315   the signal averaging period from 22:45 to 23:45 UTC includes cloud-free section. Three gravity

316   waves obviously crossed the lidar field site and triggered ice nucleation just before 23 UTC, 15-

317   30 minutes after 23 UTC, and around mid night (00:00 UTC). The temperature at cloud top at

318   about 8.5-8.6 km height was close to -35°C. For this high temperature and the high particle

319   surface area concentration of 200 µm^2/cm^3 (see Fig.10d, thin blue line) we yield smoke INP

320   concentrations of 1-10 L^{-1} for a relatively low ice supersaturation of 1.30-1.33 and an updraft

321   period of 600 s. Again, a depletion of the INP reservoir is visible after formation of the cirrus

322   layer (see Figs.6c and 6d around and above 8.5 km height).

323

324   **Conclusion**

325   The operation of a fluorescence channel in the LILAS lidar during strong smoke events in

326   the summer and autumn seasons of 2020 has demonstrated the ability of the fluorescence lidar

327   technique to monitor smoke layers in the UTLS height range in large detail. The fluorescence

328   capacity G_F of smoke particles during this period varied within a relatively small range: 2.8-

329   4.5×10^{-4}, thus the use of the mean value of G_F allows to estimate the contribution of smoke to the

330   total particle backscattering coefficient. The fluorescence lidar technique makes it possible to

331   estimate smoke parameters, such as number, surface area and volume concentration in UTLS

332   height range in a quantitative way by applying conversion factors (C_N, C_S, $C_{V)}$ which link the

333   fluorescence backscattering and the smoke microphysical properties. These factors, derived from

334   the synergy of multiwavelength Mie-Raman and fluorescence lidar observations, show some

335   variation from episode to episode, however, the use of mean values of C_N, C_S, C_V allow

336   estimation of smoke properties in UTLS height regime with reasonable accuracy. Based on two

337   case studies, we demonstrated that the fluorescence lidar technique provides the unique

338   possibility to characterize the smoke particles and their amount inside cirrus cloud layers. The

339   smoke input parameter (surface area concentration) in smoke INP parameterization schemes that

340   are used to predict ice crystal number concentrations in cirrus generation cells, can now be

341   estimated within freshly formed cirrus layers.

342   The smoke parameters such as fluorescence capacity and conversion factors were derived

343   from observations of aged wildfire smoke, transported over Atlantic in 2020. However, smoke

344   composition, depends on many factors, such as burning materials type, flame temperature and

345   environmental conditions, thus the smoke fluorescence properties may also vary. Hence, it is

346   important to perform the measurements for different locations and seasons. The fluorescence

347   backscattering in UTLS height range is quite weak, so to perform measurements with higher

348   temporal resolution more powerful lidar systems are needed. A dedicated high power Lidar,

349   LIFE (Laser Induced Fluorescence Explorer), will be designed and operated at ATOLL, in the

350   frame of OBS4CLIM/ACTRIS-France . .

351

352

Atmospheric
Chemistry
and Physics
Discussions
Open Access
EGU

359 identification and for assistance with the pollen data handling. Development of algorithm for
360 analysis of fluorescence observations was supported by Russian Science Foundation (project 21-
361 17-00114). ESA/QA4EO program is greatly acknowledged for his support to the observation
362 activity at LOA.

363

364 **References**

365 Ansmann, A., Riebesell, M., Wandinger, U., Weitkamp, C., Voss, E., Lahmann, W., and
366   Michaelis, W.: Combined Raman elastic-backscatter lidar for vertical profiling of moisture,
367   aerosols extinction, backscatter, and lidar ratio, Appl.Phys.B, *55*, 18-28, 1992.

368 Ansmann, A., Baars, H., Chudnovsky, A., Mattis, I., Veselovskii, I., Haarig, M., Seifert, P.,
369   Engelmann, R., and Wandinger, U.: Extreme levels of Canadian wildfire smoke in the
370   stratosphere over central Europe on 21–22 August 2017, Atmos. Chem. Phys., 18, 11831–
371   11845, 2018. https://doi.org/10.5194/acp-18-11831-2018.

372 Ansmann, A., Mamouri, R.-E., Hofer, J., Baars, H., Althausen, D., and Abdullaev, S. F.: Dust
373   mass, cloud condensation nuclei, and ice-nucleating particle profiling with polarization lidar:
374   updated POLIPHON conversion factors from global AERONET analysis, Atmos. Meas.
375   Tech., 12, 4849–4865, https://doi.org/10.5194/amt-12-4849-2019, 2019a.

376 Ansmann, A., Mamouri, R.-E., Bühl, J., Seifert, P., Engelmann, R., Hofer, J., Nisantzi, A.,
377   Atkinson, J. D., Kanji, Z. A., Sierau, B., Vrekoussis, M., and Sciare, J.: Ice-nucleating particle
378   versus ice crystal number concentrationin altocumulus and cirrus layers embedded in Saharan
379   dust:a closure study, Atmos. Chem. Phys., 19, 15087–15115, https://doi.org/10.5194/acp-19-
380   15087-2019, 2019b.

381 Ansmann, A., Ohneiser, K., Mamouri, R.-E., Veselovskii, I., Knopf, D. A., Baars, H.,
382   Engelmann, R., Foth, A., Jimenez, C., Seifert, P., and Barja, B.: Tropospheric and
383   stratospheric wildfire smoke profiling with lidar: Mass, surface area, CCN and INP retrieval,
384   Atmos. Chem. Phys., 21, 9779–9807, 2021. https://doi.org/10.5194/acp-21-9779-2021.

385 Baars, H., Ansmann, A., Ohneiser, K., Haarig, M., Engelmann, R., Althausen, D., Hanssen, I.,
386   Gausa, M., Pietruczuk, A., Szkop, A., Stachlewska, I. S., Wang, D., Reichardt, J., Skupin, A.,
387   Mattis, I., Trickl, T., Vogelmann, H., Navas-Guzmán, F., Haefele, A., Acheson, K., Ruth, A.
388   A., Tatarov, B., Müller, D., Hu, Q., Podvin, T., Goloub, P., Veselovskii, I., Pietras, C.,

389   Haeffelin, M., Fréville, P., Sicard, M., Comerón, A., Fernández García, A. J., Molero
390   Menéndez, F., Córdoba-Jabonero, C., Guerrero-Rascado, J. L., Alados-Arboledas, L., Bortoli,
391   D., Costa, M. J., Dionisi, D., Liberti, G. L., Wang, X., Sannino, A., Papagiannopoulos, N.,
392   Boselli, A., Mona, L., D'Amico, G., Romano, S., Perrone, M. R., Belegante, L., Nicolae, D.,
393   Grigorov, I., Gialitaki, A., Amiridis, V., Soupiona, O., Papayannis, A., Mamouri, R.-E.,
394   Nisantzi, A., Heese, B., Hofer, J., Schechner, Y. Y., Wandinger, U., and Pappalardo, G.: The
395   unprecedented 2017–2018 stratospheric smoke event: decay phase and aerosol properties
396   observed with the EARLINET, Atmos. Chem. Phys., 19, 15183–15198,
397   https://doi.org/10.5194/acp-19-15183-2019, 2019.
398   Baars, H., Radenz, M., Floutsi, A. A., Engelmann, R., Althausen, D., Heese, B., Ansmann, A.,
399   Flament, T., Dabas, A., Trapon, D., Reitebuch, O., Bley, S., and Wandinger, U.: Californian
400   wildfire smoke over Europe: A first example of the aerosol observing capabilities of Aeolus
401   compared to ground-based lidar. Geophysical Research Letters, 48, e2020GL092194.
402   https://doi.org/10.1029/2020GL092194, 2021.
403   Barahona, D., Molod, A., and Kalesse, H.: Direct estimation of the global distribution of vertical
404   velocity within cirrus clouds, Sci. Rep., 7, 20 6840, https://doi.org/10.1038/s41598-017-
405   07038-6, 2017.
406   Boose, Y., Sierau, B., Garcia, M. I., Rodriguez, S., Alastuey, A., Linke, C., Schnaiter, M.,
407   Kupiszewski, P., Kanji, Z. A., and Lohmann, U.: Ice nucleating particles in the Saharan Air
408   Layer, Atmos. Chem. Phys., 16, 9067-9087, https://doi.org/10.5194/acp-16-9067-2016, 2016.
409   China, S., Alpert, P. A., Zhang, B., Schum, S., Dzepina, K., Wright, K., Owen, R. C., Fialho, P.,
410   Mazzoleni, L. R., Mazzoleni, C., and Knopf, D. A.: Ice cloud formation potential by free
411   tropospheric particles from long-range transport over the Northern Atlantic Ocean, J.
412   Geophys. Res.-Atmos., 122, 3065–3079, https://doi.org/10.1002/2016JD025817, 2017.
413   DeMott, P. J., Prenni, A. J., Liu, X., Kreidenweis, S. M., Petters, M. D., Twohy, C. H.,
414   Richardson, M. S., Eidhammer, T., and Rogers, D. C.: Predicting global atmospheric ice
415   nuclei distributions and their impacts on climate, Proc. Natl. Acad. Sci. USA, 107, 11217–
416   11222, doi:10.1073/pnas.0910818107, 2010.
417   DeMott, P. J., Prenni, A. J., McMeeking, G. R., Sullivan, R. C., Petters, M. D., Tobo, Y.,
418   Niemand, M., Möhler, O., Snider, J. R., Wang, Z., and Kreidenweis, S. M.: Integrating

419   laboratory and field data to quantify the immersion freezing ice nucleation activity of mineral
420   dust particles, Atmos. Chem. Phys., 15, 393–409, doi:10.5194/acp-15-393-2015, 2015.

421 Fernald, F. G.: Analysis of atmospheric lidar observations: some comments, Appl. Opt., 23, 652–
422   653, doi.org/10.1364/AO.23.000652, 1984.

423 Freudenthaler,V., Esselborn, M.,Wiegner, M.,Heese, B., Tesche, M. and co-authors:
424   Depolarization ratio profiling at severalwavelengths in pure Saharan dust during SAMUM
425   2006, *Tellus* 61B, 165–179, 2009.

426 Fromm, M., Lindsey, D. T., Servranckx, R., Yue, G., Trickl, T., Sica, R., Doucet, P., and Godin-
427   Beekmann, S. E.: The untold story of pyrocumulonimbus, B. Am. Meteorol. Soc., 91, 1193–
428   1209, https://doi.org/10.1175/2010bams3004.1, 2010.

429 Grawe, S., Augustin-Bauditz, S., Hartmann, S., Hellner, L., Pettersson, J. B. C., Prager, A.,
430   Stratmann, F., and Wex, H.: The immersion freezing behavior of ash particles from wood and
431   brown coal burning, Atmospheric Chemistry and Physics, 16, 13 911–13 928, 2016.
432   https://doi.org/10.5194/acp-16-13911-2016.

433 Haarig, M., Ansmann, A., Baars, H., Jimenez, C., Veselovskii, I., Engelmann, R., and Althausen,
434   D.: Depolarization and lidar ratios at 355, 532, and 1064 nm and microphysical properties of
435   aged tropospheric and stratospheric Canadian wildfire smoke, Atmos. Chem. Phys., 18,
436   11847-11861, https://doi.org/10.5194/acp-18-11847-2018, 2018.

437 Holben, B. N., Eck, T. F., Slutsker, I., Tanré, D., Buis, J. P., Setzer, A., Vermote, E., Reagan, J.
438   A., Kaufman, Y. J., Nakajima, T., Lavenu, F.,Jankowiak, I., and Smirnov, A.: AERONET – a
439   federated instrument network and data archive for aerosol characterization, Remote Sens.
440   Environ., 66, 1–16, 1998.

441 Hoose, C. and Möhler, O.: Heterogeneous ice nucleation on atmospheric aerosols: a review of
442   results from laboratory experiments. Atmos. Chem. Phys., 12, 9817–9854, 2012.
443   doi:10.5194/acp-12-9817-2012

444 Hu, Q., Goloub, P., Veselovskii, I., Bravo-Aranda, J.-A., Popovici, I. E., Podvin, T., Haeffelin,
445   M., Lopatin, A., Dubovik, O., Pietras, C., Huang, X., Torres, B., and Chen, C.: Long-range-
446   transported Canadian smoke plumes in the lower stratosphere over northern France, Atmos.
447   Chem. Phys., 19, 1173-1193, 2019. https://doi.org/10.5194/acp-19-1173-2019.

448   Jahl, L. G., Brubaker, T. A., Polen, M. J., Jahn, L. G., Cain, K. P., Bowers, B. B., Fahy, W. D.,

449   Graves, S., and Sullivan, R. C.: Atmospheric aging enhances the ice nucleation ability of

450   biomass-burning aerosol, Science Advances, 7, eabd3440, 2021.

451   Kanji, Z. A., Ladino, L. A., Wex, H., Boose, Y., Burkert-Kohn, M., Cziczo, D. J., and Krämer,

452   M.: Chapter 1: Overview of ice nucleating particles, Meteor Monogr., Am. Meteorol. Soc.,

453   58, 1.1-1.33, https://doi.org/10.1175/amsmonographs-d-16-0006.1, 2017.

454   Khaykin, S., Legras, B., Bucci, S., Sellitto, P., Isaksen, L., Tencé, F., Bekki, S., Bourassa, A.,

455   Rieger, L., Tawada, D., Jumelet, J., and Godin-Beekmann, S.: The 2019/20 Australian

456   wildfires generated a persistent smoke-charged vortex rising up to 35 km altitude, Commun.

457   Earth Environ., 1, 22, https://doi.org/10.1038/s43247-020-00022-5, 2020.

458   Klett J.D., "Lidar inversion with variable backscatter/extinction ratios", Appl.Opt. 24, 1638-

459   1643, 1985.

460   Knopf, D. A., Alpert, P. A., and Wang, B.: The role of organic aerosol in atmospheric ice

461   nucleation: a review, ACS Earth and Space Chemistry, 2, 168–202, 2018.

462   Müller, D., Wandinger, U., and Ansmann, A.: Microphysical particle parameters from extinction

463   and backscatter lidar data by inversion with regularization: theory, Appl. Opt. 38, 2346-2357,

464   1999.

465   Müller, D., Mattis, I., Wandinger, U., Ansmann, A., Althausen, A., and Stohl, A.: Raman lidar

466   observations of aged Siberian and Canadian forest fire smoke in the free troposphere over

467   Germany in 2003: Microphysical particle characterization, J. Geophys. Res., 110, D17201,

468   doi:10.1029/2004JD005756, 2005.

469   Murray, B. J., O'Sullivan, D., Atkinson, J. D., and Webb, M. E.: Ice nucleation by particles

470   immersed in supercooled cloud droplets, Chem. Soc. Rev., 41, 6519–6554,

471   https://doi.org/10.1039/c2cs35200a, 2012.

472   Ohneiser, K., Ansmann, A., Engelmann, R., Ritter, C., Chudnovsky, A., Veselovskii, I., Baars,

473   H., Gebauer, H., Griesche, H., Radenz, M., Hofer, J., Althausen, D., Dahlke, S., and Maturilli,

474   M.: Siberian fire smoke in the High-Arctic winter stratosphere observed during MOSAiC

475   2019–2020, Atmos. Chem. Phys. Discuss. [preprint], https://doi.org/10.5194/acp-2021-117, in

476   review, 2021.

477 Peterson, D. A., Campbell, J. R., Hyer, E. J., Fromm, M. D., Kablick, G. P., Cossuth, J. H., and

478   DeLand, M. T.: Wildfire-driven thunderstorms cause a volcano-like stratospheric injection of

479   smoke, npj Clim. Atmos. Sci., 1, 30, https://doi.org/10.1038/s41612-018-0039-3, 2018

480 Pérez-Ramírez, D., Whiteman, D. N., Veselovskii, I., Kolgotin, A., Korenskiy, M., and

481   Alados-Arboledas, L.: Effects of systematic and random errors on the retrieval of particle

482   microphysical properties from multiwavelength lidar measurements using inversion with

483   regularization, Atmos. Meas. Tech., 6, 3039-3054, 2013.

484 Prata, A.T., Young, S.A., Siems S.T., and Manton, M.J.: Lidar ratios of stratospheric volcanic

485   ash and sulfate aerosols retrieved from CALIOP measurements Atmos. Chem. Phys., 17,

486   8599–8618, 2017. https://doi.org/10.5194/acp-17-8599-2017

487 Reichardt, J., Leinweber, R., Schwebe, A.: Fluorescing aerosols and clouds: investigations of co-

488   existence, Proceedings of the 28th ILRC, Bucharest, Romania, 25-30 June, 2017.

489 Schrod, J., Weber, D., Drücke, J., Keleshis, C., Pikridas, 5 M., Ebert, M., Cvetkovic´, B.,

490   Nickovic, S., Marinou, E., Baars, H., Ansmann, A., Vrekoussis, M., Mihalopoulos, N., Sciare,

491   J., Curtius, J., and Bingemer, H. G.: Ice nucleating particles over the Eastern Mediterranean

492   measured by unmanned aircraft systems, Atmos. Chem. Phys., 17, 4817-4835,

493   https://doi.org/10.5194/acp-17-4817-2017, 2017.

494 Umo, N. S., Murray, B. J., Baeza-Romero, M. T., Jones, J. M., Lea-Langton, A. R., Malkin, T.

495   L., O'Sullivan, D., Neve, L., Plane, J. M. C., and Williams, A.: Ice nucleation by combustion

496   ash particles at conditions relevant to mixed-phase clouds, Atmospheric Chemistry and

497   Physics, 15, 5195–5210, https://doi.org/10.5194/acp-15-5195-2015,

498 Venable, D. D., Whiteman, D. N., Calhoun, M. N., Dirisu, A.O., Connell, R. M., Landulfo, E.:

499   Lamp mapping technique for independent determination of the water vapor mixing ratio

500   calibration factor for a Raman lidar system, Appl. Opt., 50, 4622 - 4632, 2011.

501 Veselovskii I., Kolgotin, A., Griaznov, V., Müller, D., Wandinger, U., Whiteman, D.:

502   Inversion with regularization for the retrieval of tropospheric aerosol parameters from multi-

503   wavelength lidar sounding, Appl.Opt. 41, 3685-3699, 2002.

504 Veselovskii, I., Whiteman, D. N., Korenskiy, M., Suvorina, A., Kolgotin, A., Lyapustin, A.,

505   Wang, Y., Chin, M., Bian, H., Kucsera, T. L., Pérez-Ramírez, D., and Holben, B.:

506   Characterization of forest fire smoke event near Washington, DC in summer 2013 with

507   multiwavelength lidar, Atmos. Chem. Phys., 15, 1647-1660, https://doi.org/10.5194/acp-15-
508   1647-2015, 2015.

509   Veselovskii, I., Hu, Q., Goloub, P., Podvin, T., Korenskiy, M., Pujol, O., Dubovik, O., Lopatin,
510   A.: Combined use of Mie-Raman and fluorescence lidar observations for improving aerosol
511   characterization: feasibility experiment, Atm. Meas. Tech., 13, 6691–6701, 2020.
512   doi.org/10.5194/amt-13-6691-2020.

513   Veselovskii, I., Hu, Q., Goloub, P., Podvin, T., Choël, M., Visez, N., and Korenskiy, M.: Mie–
514   Raman–fluorescence lidar observations of aerosols during pollen season in the north of
515   France, Atm. Meas. Tech., 14, 4773–4786, 2021. doi.org/10.5194/amt-14-4773-2021

516

517 Table 1. Conversion factors C_N, C_S, and C_V, and fluorescence capacity G_F at height H for five
518 smoke episodes. Volume and surface area concentration of smoke particles, obtained by the
519 inversion of $3\beta+2\alpha$ lidar observations (V, S), are given together with values calculated from
520 fluorescence measurements (V_F, S_F) and using conversion factors (Eq. 4).

Date dd/mm/yy	H, km	C_N, $10^4 \frac{cm^{-3}}{Mm^{-1}sr^{-1}}$	C_S, $10^4 \frac{\mu m^2 cm^{-3}}{Mm^{-1}sr^{-1}}$	C_V, $10^4 \frac{\mu m^3 cm^{-3}}{Mm^{-1}sr^{-1}}$	G_F, 10^{-4}	V, $\mu m^3/cm^3$		S, $\mu m^2/cm^3$	
						V	V_F	S	S_F
23/06/20	4.9	88	35	2.4	3.5	21	19	306	237
11/09/20	7.5	75	28	2.0	3.9	7.6	8.7	111	111
14/09/20	6.0	90	34	2.3	3.7	6.4	6.1	94	78
17/09/20	6.8	21	21	2.3	2.9	8.0	7.8	73	100
20/09/20	4.9	33	22	2.0	4.3	2.7	2.9	31	37

521
522
523
524
525
526 Table 2. Number N, surface area S, and volume V concentrations of smoke particles inside the

527 ice cloud at height H estimated from fluorescence measurements by applying the conversion

528 factors in Eq. (4) for four measurement sessions.

| Date dd/mm/yy	Time UTC	H, km	β_F, 10^{-4} Mm^{-1}sr^{-1}	N, cm^{-3}	S, $\mu m^2/cm^3$	V, $\mu m^3/cm^3$
12/09/20	01:20-01:45	10.5	0.32	20±10	9±2.3	0.7±0.07
12-13/09/20	21:00-03:00	12.5	0.06	3.5±1.8	1.6±0.4	0.13±0.013
17/09/20	22:45-23:45	8.5	6.5	400±200	180±45	14±1.4
24-25/11/20	18:00-06:00	8.0	0.013	0.8±0.4	0.36±0.09	0.03±0.003

529
530

531

532

533
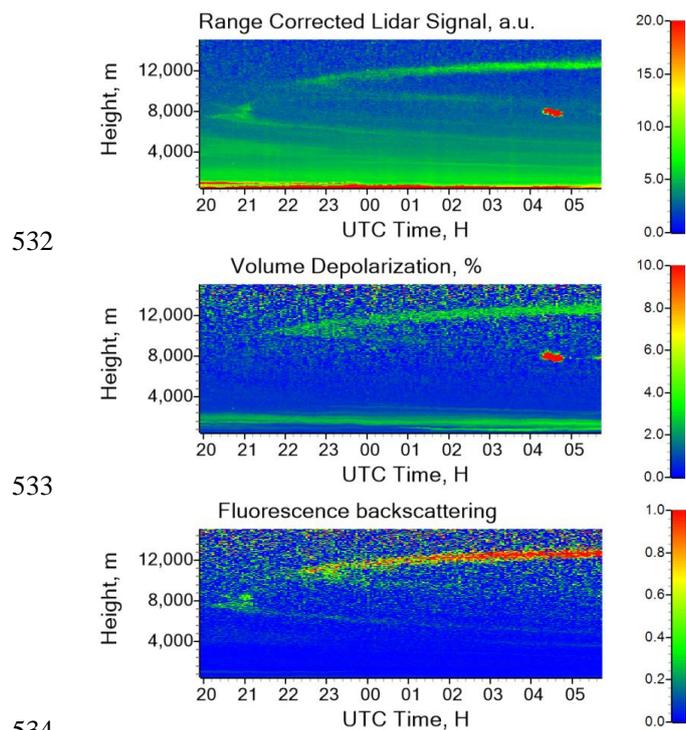
534
535 Fig.1. Range corrected lidar signal at 1064 nm, volume depolarization ratio at 1064 nm and
536 fluorescence backscattering coefficient (in 10^{-4} $Mm^{-1}sr^{-1}$) on 4-5 November 2020.
537
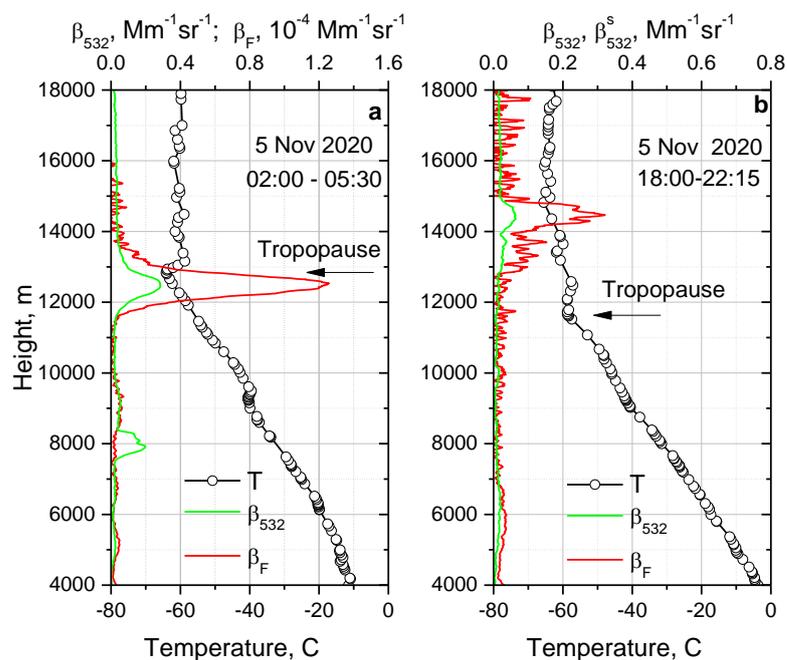
538
539   Fig.2. Vertical profiles of aerosol backscattering β_{532} and fluorescence backscattering β_F
540   coefficients on 5 November 2020 for the periods (a) 02:00 - 5:30 UTC and (b) 18:00 – 22:15
541   UTC. Open symbols show the temperature profile measured by the radiosonde launched at
542   Herstmonceux (UK).
543
544

545
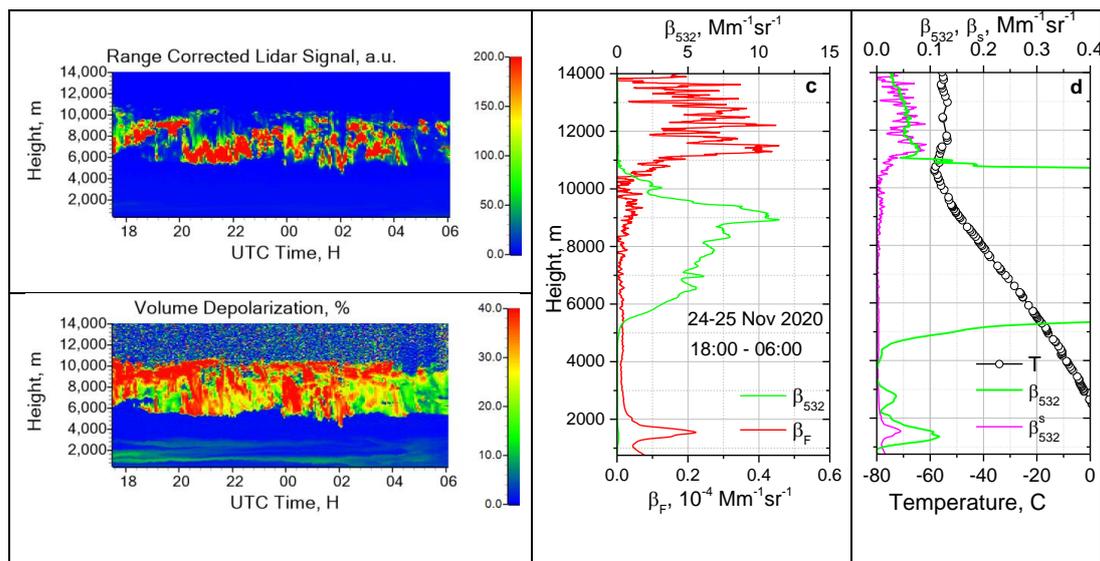
546
547 Fig.3. Smoke fluorescence in the presence of clouds on 24 – 25 November 2020. (a, b) Height –
548 temporal distribution of the range corrected lidar signal and volume depolarization at 1064 nm.
549 (c) Vertical profiles of the aerosol β_{532} and fluorescence β_F backscattering coefficients. (d)
550 Aerosol backscattering β_{532} together with smoke backscattering β_{532}^s coefficient, computed from
551 β_F for $G_F=4.5\times10^{-4}$. Open symbols show temperature profile measured by the radiosonde at
552 Herstmonceux.
553
554

555
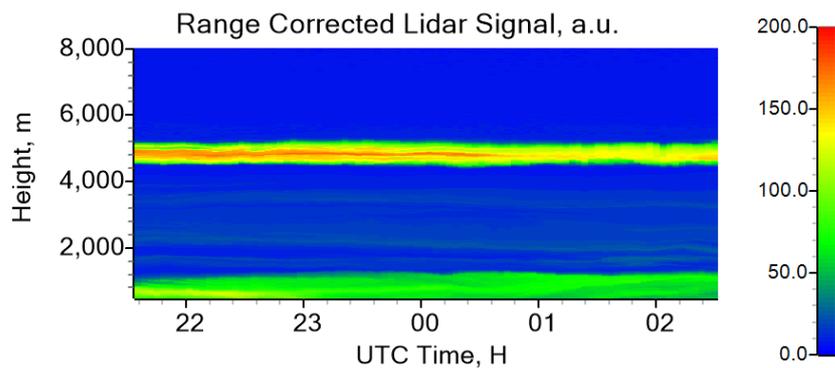
556
557   Fig.4. Range corrected lidar signal at 1064 nm on 23-24 June 2020, indicating a thick smoke
558   layer between 4500 and 5200 m height.
559

560
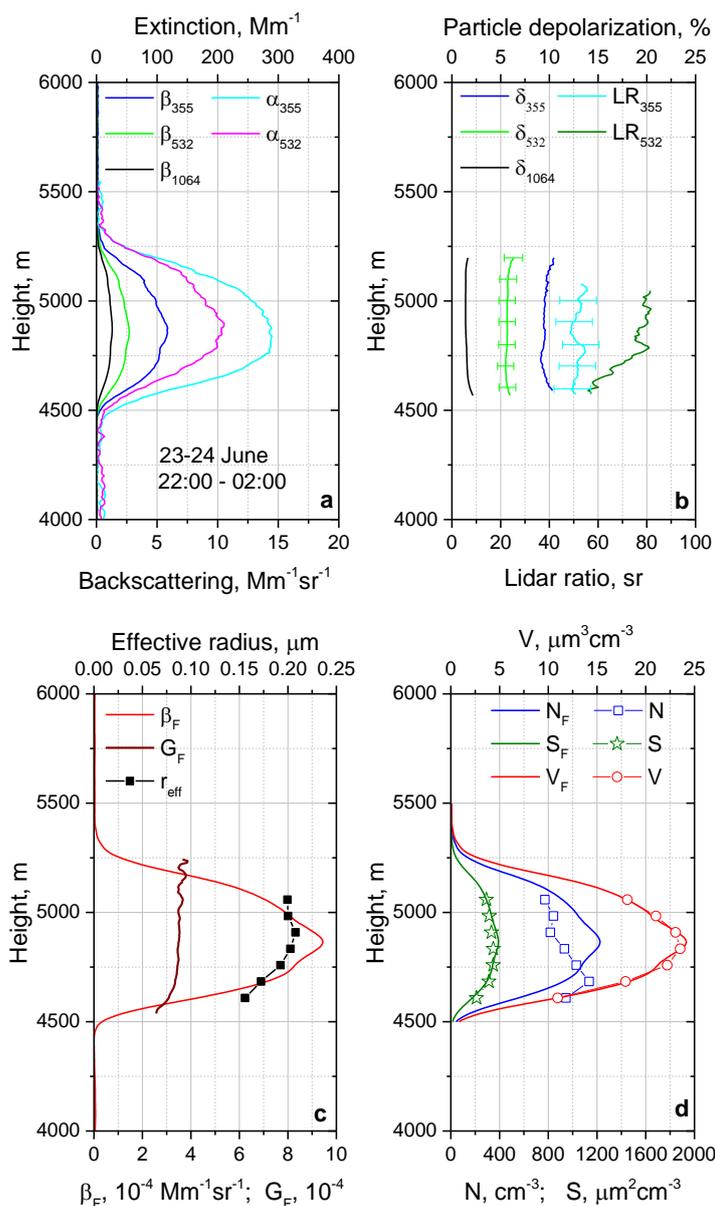
561
562
Fig.5. Smoke layer on 23-24 June 2020. (a) Vertical profiles of backscattering (β_{355}, β_{532}, β_{1064})
and extinction (α_{355}, α_{532}) coefficients. (b) Particle depolarization ratios (δ_{355}, δ_{532}, δ_{1064}) and lidar
ratios (LR$_{355}$, LR$_{532}$). (c) Fluorescence backscattering (β_F), fluorescence capacity (G_F) and the
particle effective radius (r_{eff}). (d) Number (N, N_F), surface area (S, S_F) and volume (V, V_F)
concentrations obtained by inversion of $3\beta+2\alpha$ observations (symbols) and calculated from the
fluorescence backscattering (lines) by using the mean conversion factors defined in Eq. (3).
569
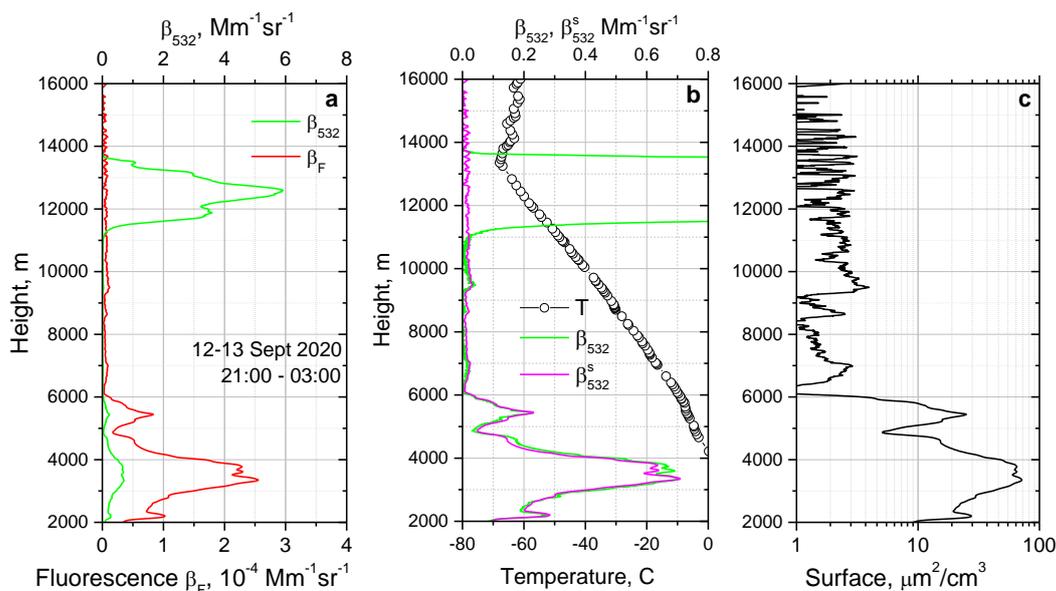
570
571 Fig.6. Observation of smoke fluorescence on 12-13 September 2020, 21:00 – 03:00 UTC. (a)
572 Vertical profiles of the aerosol backscattering β_{532} and fluorescence backscattering β_F
573 coefficients. (b) Aerosol backscattering β_{532} together with smoke backscattering β_{532}^s coefficient
574 computed from β_F for $G_F=3.6\times10^{-4}$. (c) Surface area concentration of the smoke particles
575 calculated from β_F by using the respective conversion factor in Eq. (4). Open symbols show the
576 temperature profile measured by the radiosonde at Herstmonceux.
577
578
579

Atmospheric
Chemistry
and Physics
Discussions

Open Access

EGU

580

581

582
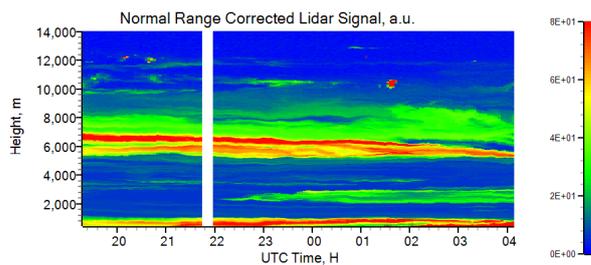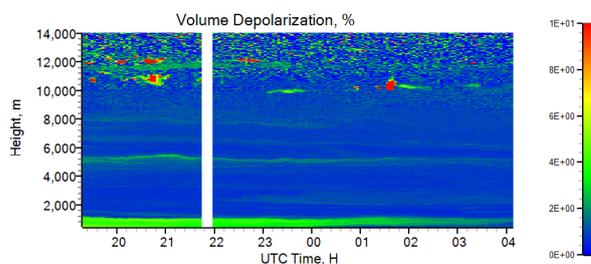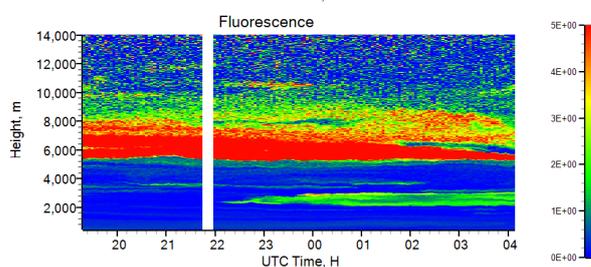
583
584 Fig.7. Formation of ice particles at heights above 10 km inside a smoke layer on 11-12 September 2020.
585 (a) Range corrected lidar signal at 1064 nm, (b) volume depolarization ratio at 1064 nm and (c)
586 fluorescence backscattering coefficient (in 10^{-4} $Mm^{-1}sr^{-1}$).
587
588

Fig.8. Formation of ice particles at 10-11 km height inside a smoke layer on 11-12 September 2020. Vertical profiles (a, d) of aerosol backscattering coefficients β_{355}, β_{532}, β_{1064}; (b, e) the particle depolarization ratios δ_{355}, δ_{532}, δ_{1064}; (c, f) backscattering coefficient β_{532} together with backscattering coefficient of smoke β_{532}^s, calculated from fluorescence backscattering β_F assuming G_F=4.0×10^{-4}. Plot (f) shows also the surface area concentration S of the smoke particles calculated from β_F by applying the respective conversion factor in Eq. (4). Results are given for the time intervals 23:00 – 00:30 UTC and 01:20 – 01:45 UTC: prior and during ice cloud formation at 10.5 km height. The temperature profile measured by the radiosonde at Herstmonceux is shown with open symbols in panel (c).
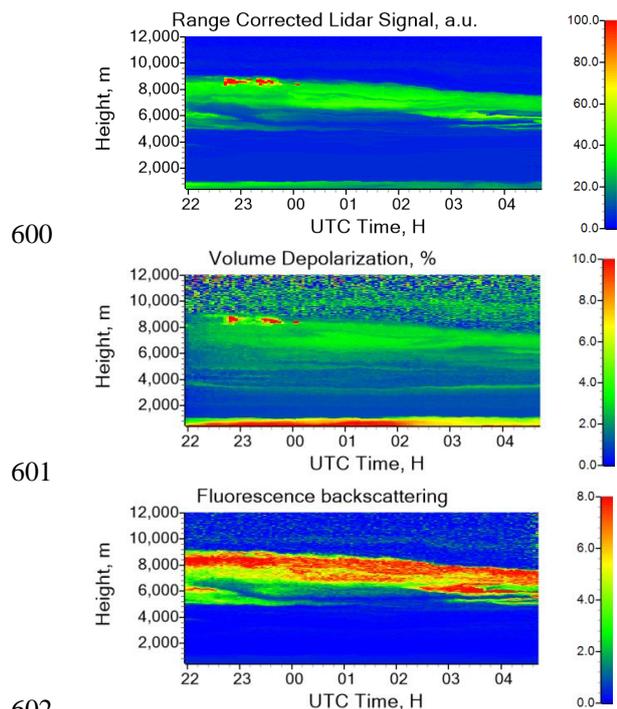
Fig.9. Formation of ice particles at heights above 8 km inside the smoke layer on 17-18 September 2020. (a) Range corrected lidar signal at 1064 nm, (b) volume depolarization ratio at 1064 nm and (c) fluorescence backscattering coefficient (in 10^{-4} $Mm^{-1}sr^{-1}$).

609

610

611
612
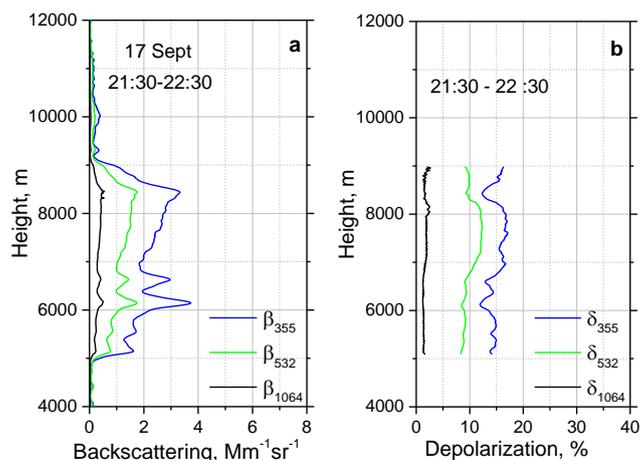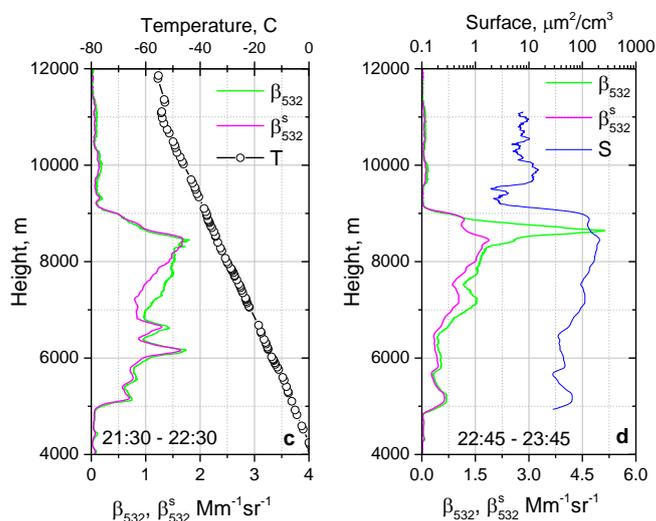
Fig.10. Formation of ice particles at 8.5-8.6 km height inside a smoke layer on 17 September 2020. Vertical profiles of (a) aerosol backscattering coefficients β_{355}, β_{532}, β_{1064}; (b) the particle depolarization ratios δ_{355}, δ_{532}, δ_{1064}; (c, d) backscattering coefficient β_{532} together with backscattering coefficient of smoke β_{532}^s, calculated from fluorescence backscattering β_F assuming $G_F=3.5\times10^{-4}$. Results are given for the time intervals (a-c) 21:30 – 22:30 UTC and (d) 22:45 – 23:45 UTC: prior and during ice formation at 8.5 km height. Plot (d) shows also the surface area concentration of the smoke particles calculated from β_F and by applying the respective conversion factor in Eq. (4). The temperature profile measured by the radiosonde at Herstmonceux is shown with open symbols in panel (c).

622